

Solar Light-Driven Photocatalysis Using BaFe₂O₄/rGO for Chlorhexidine Digluconate Contaminated Water: Comparison With Artificial UV and Visible Light-Mediated Photocatalysis

Astha Singh

Indian Institute of Technology (Indian School of Mines): Indian Institute of Technology

Brijesh Kumar Mishra (✉ bkmishra3@rediffmail.com)

Indian Institute of Technology (ISM) <https://orcid.org/0000-0002-4451-1924>

Research Article

Keywords: Chlorhexidine Digluconate, BaFe₂O₄/rGO, Adsorption combining Photocatalysis, Energy Efficiency

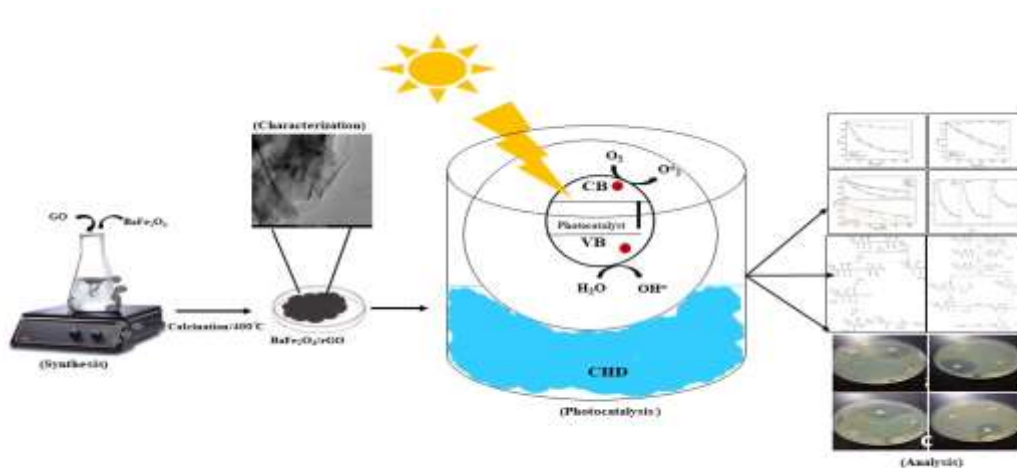
Posted Date: April 28th, 2021

DOI: <https://doi.org/10.21203/rs.3.rs-386420/v1>

License: © ⓘ This work is licensed under a Creative Commons Attribution 4.0 International License.

[Read Full License](#)

Version of Record: A version of this preprint was published at Environmental Science and Pollution Research on January 7th, 2022. See the published version at <https://doi.org/10.1007/s11356-021-17689-8>.



28
29
30
31
32
33
34

Keywords: Chlorhexidine Digluconate; BaFe₂O₄/rGO; Adsorption combining Photocatalysis; Energy Efficiency

35 **Highlights**

36
37
38
39
40
41
42
43
44

- The adsorption and photocatalysis efficiency of BaFe₂O₄/rGO as catalyst displayed excellent degradation performance to CHD through π - π stacking.
- Reduction in UV₂₅₄ also confirmed that the mineralized end product by BaFe₂O₄/rGO has excellent degradation efficiency.
- Photogenerated electrons and Hydroxyl radicals was substantially responsible for CHD degradation.
- Toxicity of parent compound and its by-products reduces after photocatalysis process in BaFe₂O₄/rGO and possible pathway were established.

45
46 **1. Introduction**

47 Extensive research has focused on photocatalytic degradation of Personal Care Products (PCPs) due
48 to their recalcitrant nature, nonbiodegradability, and unregulated disposal into aquatic bodies. These
49 compounds, thus, negatively impact on both environment and human health (Das et al., 2014).
50 Chlorhexidine Digluconate (CHD), which is a model compound, is broadly used as antiseptic among
51 PCPs. It is commonly present in disinfectant, mouthwash formulations, toothpaste and cosmetics due
52 to effectiveness against Gram-positive and Gram-negative bacteria (Sousa et al., 2017). CHD consist

53 of two hexanes bonded (p-chlorophenyl) biguanides and its primary degradation product p-
54 chloroaniline act as a limiting factor for stabilizing the compound. However, overuse of these
55 compound have been frequently detected in water bodies and are quickly absorbed/ metabolized as
56 both hemotoxic and carcinogenic(Nidhi et al., 2011). Due to complex structure and bacteriostatic
57 properties of CHD molecules, it can neither be completely removed through conventional treatment
58 technologies from wastewater nor be biodegraded from the environment (Zwiener and Frimmel,
59 2000).

60 Thus, the development of efficient technologies are highly desired to remove PCPs and
61 pharmaceuticals such as CHD from the aquatic ecosystem (Fidelis et al., 2019). Adsorption is an
62 efficient and economical treatment for organic pollutant but with some limitations such as inefficient
63 in complete degradation and leads to the secondary pollutant. Recently, graphene oxide (GO) with
64 high surface area, strong functional group and conjugate π region used as an adsorbent for organic
65 pollutant removal (Zhang et al., 2016).Undoubtedly, adsorption process can only change the phase of
66 the pollutant, cannot completely remove the organic pollutant. In addition, photocatalysis is an
67 efficient and green technology for mineralization of recalcitrant organic pollutant with some
68 advantages such as lack of secondary waste generation and easy implementation (Wang et al., 2021).
69 Interestingly, studies showed that use of adsorption-photocatalysis simultaneously grab attention for
70 efficient removal of organic pollutant due to recombination of electron-hole pair disadvantage of
71 photocatalysis (Yuan et al., 2020). Various studies showed significant removal of antibiotics using
72 adsorption-photocatalysis treatment such as ciprofloxacin (with 59.5% adsorption and 82.5 %
73 degradation in 60 min), tetracycline (with 18% adsorption and 70% degradation in 90 min), ofloxacin
74 (with 93.4% adsorption and photocatalytic degradation in 30 min) (Chen et al., 2020).Motivated by
75 previous studies, Barium ferrites with exceptional magnetic and photocatalytic property used for
76 synthesis of new material in order to develop the dual functioning material by combining the
77 advantages of both adsorption-photocatalysis technologies (Roonasi and Mazinani, 2017a). As per the
78 literature, barium ferrites have less been studied and can also be used for easy separation as well as
79 strong visible light absorption capacity due to narrower band gap (Casbeer et al., 2012).

80 In this system, Response surface methodology (RSM) has been used to understand the interaction
81 among the operating conditions (pH, catalyst dose and time) for optimization process, resulting in a
82 good estimate of the optimum response BaFe₂O₄/rGO used as an adsorbent first in dark, and as
83 photocatalyst under UV, visible and solar radiation. In addition, kinetic studies for removal of
84 pollutant, mineralization rate (in terms of TOC) and reduction in aromaticity (in terms of
85 UV₂₅₄/UV₂₈₀) during adsorption and photocatalysis has been carried out. Furthermore, possible
86 mechanism for mineralization of pollutant via adsorption-photocatalysis was studied by trapping
87 experiment and possible pathway was proposed, based on LC-MS analysis. For practical applicability,

88 BaFe₂O₄/rGO photocatalyst used for the treatment of formulated wastewater in UV, visible and solar
89 radiation.

90

91

92

93

94 **2. Materials and Methods**

95 **2.1. Chemicals**

96 All the chemicals and reagent were procured by Sigma-Aldrich. They were of analytical grade and
97 used without further purification. Microporous hydrophobic PTFE membrane with pore size around
98 0.45 μm and 80 % porosity was obtained from GE Osmonics Company.

99 **2.2. Syntheses of Graphene Oxide:**

100 For the present study, 1 g of graphite (Jodex England) was carefully added to the mixture of
101 concentrated H₂SO₄:H₃PO₄ (prepared in a ratio of 4:1 by v/v). After the addition of graphite, the
102 prepared solution was placed in an ice bath. Consequently, the experimentation was carried out at
103 room temperature where the prepared mixture was stirred for 72 h using a rotary shaker. The process
104 was carried out till the mixture's color changed to dark brown from dark purplish green. H₂O₂ was
105 added to the mixture to halt the oxidation process, which further changed its colour to bright yellow.
106 Moreover, remnant salts in the mixture were removed by adding of 10% HCl. The washing process
107 for the experimentation followed a simple decantation of supernatant. It was observed that during the
108 process of washing, the addition of deionized water caused exfoliation of GO, which thickens the
109 solution due to the formation of GO gel. The obtained GO gel was further dried for 24 h at 70 °C. The
110 dried GO gel was then stored in a dry place for further experimentation (Aboubaraka et al., 2017).

111 **2.3. Synthesis of BaFe₂O₄/rGO**

112 A certain amount of Barium nitrate and iron (2:1 w/w) were added into 100mL beakers using distilled
113 water at 60 °C. To this mixture, prepared graphene oxide was added in mass ratio of 1:2 w/w.
114 Afterward, the resulting suspension kept at magnetic stirrer for homogeneous mixing. Then, the
115 solution was filtered and ignited at a temperature of 400 °C for 30 min. The resultant dark brown
116 material was obtained and powdered into fine particle (Roonasi and Mazinani, 2017b).

117

118 **2.4 Characterization**

119 To prove the stability of prepared sample as a photocatalyst, following characterization were
120 employed i) X-ray diffraction (XRD) was used for phase identification on a Bruker D8 ADVANCE
121 diffractometer with Cu-Kα (λ=1.5406 Å) radiation, ii) Fourier transform infrared (FTIR) spectra was
122 used to identify the presence of functional group on Bruker Vertex- 70 by diffused reflectance
123 accessory technique, iii) morphology and structural observations were analyzed using Hitachi S-4300

124 type field emission scanning electron microscope (FE-SEM) at an electron acceleration voltage of 1
125 keV, iv) Energy-dispersive X-ray spectrometer (EDX) equipped on SEM was used to identify the
126 chemical compositions and elemental mapping of the catalyst, v) UV–vis diffuse reflectance spectra
127 (UV-DRS) was used for bandgap analysis using Perkin Elmer Lambda 900 spectrophotometer
128 equipped with an integrated sphere (BaSO₄ was used as a reference material),and vi) X-ray
129 photoelectron spectroscopy (XPS) was used to identify the oxidation state of compounds using a VG
130 250 Escalab spectrometer equipped with an Al anode (Al-K α =1486.7 eV) as an X-ray source.

131

132 **2.4. Experimental Design using Response surface Methodology**

133 RSM was used to optimize three variables (s/c ratio, pH and time) with three different levels (+1, 0
134 and -1) for maximum CHD removal as a response. The experimental design (DoE) was performed
135 based on the Face Centred Central Composite Design (FCCD) devised by Design Expert v7.0.0
136 software (SaMeep 104, State Ease, INC. Minneapolis (USA)). A total of 20 different combinations
137 were obtained with six centre points in random order according to a Central Composite Design (CCD)
138 configuration for three factors. In this analysis, Face Central Composite Design (FCCD) was used to
139 model the percentage removal of CHD as a quadratic model. “Analysis of variance” (ANOVA),
140 correlation coefficient (R²), lack of fit, CV % and adjusted coefficient of determination (R²_{adj}) were
141 used for statistical validation.

142 **2.5. Adsorption experiments**

143 The adsorption kinetics has been performed for the adsorbent in dark condition at optimized
144 condition. At a certain time- interval, suspension was collected and filtered through 0.45 μ m syringe
145 filter. The residual concentration of CHD was measured in UV-vis spectrophotometer (Lab-tech,
146 China). The adsorption capacity at equilibrium (q) was determined as

$$147 \quad q = (C_0 - C_e)V/m \quad (1)$$

148 where C_0 and C_e (mg L⁻¹) are the initial and equilibrium pollutant concentrations, respectively, V
149 represented the solution volume (L), and m (g) is the adsorbent mass.

150 The pseudo first-order kinetic model was given by:

$$151 \quad \ln(q - q_t) = \ln q - k_1 t \quad (2)$$

152 where t is time, q_t is adsorption capacity at time t , and k_1 is the pseudo-first-order rate constant.

153 The pseudo-second-order kinetic model was given by:

$$154 \quad \frac{t}{q_t} = \frac{t}{q} + \frac{1}{k_2 q^2} \quad (3)$$

155 where k_2 is the pseudo-second-order rate constant.

156 **2.6. Photocatalytic activity test**

157 The photocatalysis activity during CHD degradation was monitored in a lab-scale photoreactor under
158 UV light (PMI, India). The source of light provided by a UVC-lamp (11W, Phillip, intensity-44.4
159 mW.cm^{-2}) and visible lamp (200W, intensity- 40 mW.cm^{-2}) and natural light (intensity -50-60
160 mW.cm^{-2}) was measured by a radiometer (Delta OHM, LP-NET14). The dispersion of catalyst in a
161 500 mL solution of CHD (30 ppm) was injected into the photoreactor with aeration and operational
162 condition (pH range 6-10, S/C ratio 1.01-3.0 and Time 10-60 min.). This experiment tracked and
163 analysed the residual CHD in the reaction mixture as a function of time. To check the experimental
164 results' reproducibility, all the experimental runs were repeated three times. Where, one-hour batch
165 study was conducted with sample collection at a 5-minute interval. An aliquot was centrifuged (4 °C,
166 11,000 X g, 5 min.) and the supernatant was collected for subsequent analyses.

167

168 **2.7. Kinetic study of CHD degradation**

169 Calculating oxidant and reductant in solution is nearly impossible. Thus, the kinetic pseudo-first-order
170 model has been carried out to study the modeling CHD degradation Eqs (4) & (5).

$$171 \ln \frac{C_t}{C_o} = -K_{obs} t \quad (4)$$

$$172 r_{obs} = -k_{obs} C_{CHD} \quad (5)$$

173

174 Where, K_{obs} (Rate constant of reaction) was calculated from the slope by plotting a graph

175 between $\ln \frac{C_t}{C_o}$ versus t and r_{obs} is the observed CHD degradation rate ($\text{mg L}^{-1} \text{min}$) in the

176 photoreactor. In the above equations, the reaction rate constant (K_{obs}) can be either negative or

177 positive. Noticeably, " K_{obs} " does not include the concentration as these parameters are taken into

178 consideration (Nasseh et al., 2018).

179

180 **2.8. Analytical Method**

181 UV-vis spectrophotometer (Lab-tech, China) was used to measure the Ultraviolet (UV) absorbance at
182 254 nm, 280nm and residual CHD concentration in the reaction mixture were measured at 275 nm
183 upon the specification of spectral indices. TOC analyzer (Shimadzu 5000) was used to determine the
184 reduction of organic content and mineralization of CHD. LC-MS analysis (Thermo Scientific TSQ
185 8000 liquid chromatograph-mass spectrometer) has been carried out to investigate the degradation
186 products of CHD.

187 The figure-of-merit electrical energy per order (EEO) is useful for evaluating electrical energy
188 consumption in photocatalytic degradation of organic contaminants, as per International Union of
189 Pure and Applied Chemistry (IUPAC). EEO defined as amount of electrical energy consumed (kWh)
190 during photocatalytic degradation of fixed volume of organic pollutant (Azarpira et al., 2019).

$$191 \quad E_{EO} = \frac{P \times t \times 1000}{V \times 60 \times \log \frac{C_i}{C_f}} \quad (6)$$

192 Where P is the power rate (kW) of the photocatalytic system, t is the irradiation time (min), V is the
193 volume (L) of the sample.

194

195 **2.9. Bacterial susceptibility test for CHD degradation and photo mineralized product**

196 A bacterial susceptibility test was carried out on anaerobic gram-positive bacteria (*Bacillus cereus*) to
197 evaluate the potential for aquatic toxicity of treated and untreated CHD containing water. The
198 susceptibility test was carried out by autoclaving agar media of Muller Hinton, and Petri plates at
199 66.8Pa and 121 °C for 20 min. Approximately 1ml of cultural broth suspension of *Bacillus cereus* were
200 mixed in a media. Homogeneously mixed cultural suspension of bacteria and media shows a confluent
201 lawn of growth on incubation. The incubation period for bacterial growth was carried out for 24hr at
202 37 °C prior to observation of the inhibition zone.

203

204 **3. Results and discussion**

205 **3.1 Characterization of the synthesized photocatalyst**

206 The synthesized catalysts were characterized to know the bandgap, surface morphology, elemental
207 analysis, and crystallinity. UV-vis diffuse reflectance spectroscopy was used to determine optical
208 absorbance property of prepared sample and their light-harvesting nature in the wavelength visible
209 range (200-800 nm). Both the GO and BaFe₂O₄/rGO can absorb visible light but BaFe₂O₄/rGO shows
210 strong absorption in visible range due to the shifting of red absorption peak and low bandgap energy
211 was calculated using the following formula:

$$212 \quad E_g \text{ (eV)} = \frac{1240}{\lambda_g} \text{ nm}$$

213 Where λ_g is the wavelength value obtained from UV-DRS spectra. The bandgap energy has been
214 calculated from Tauc plot of absorbance data (Fig.1c), which show the improvement of the
215 photocatalytic performance of both synthesized photocatalyst (GO and BaFe₂O₄/rGO). The lowering
216 of band energy in GO (2.89eV) and BaFe₂O₄/rGO (1.86 eV) showed that the synthesis process has
217 been achieved successfully. DRS results of GO revealed the absorption peak of $\pi \rightarrow \pi^*$ transition of C-

218 C bonds around 210-203 nm along with another peak of $n \rightarrow \pi^*$ transition of C-O bonds around 300-
219 320 nm. However, in BaFe₂O₄/rGO, $\pi \rightarrow \pi^*$ transition peak has been shifted around 260-270 nm
220 demonstrating the restoration of electronic conjugation on functionalization of GO. Therefore,
221 BaFe₂O₄/rGO can effectively improve the light absorption properties of GO, for visible range as well.
222

223 **Fig. 1:** a) XRD patterns; b) FTIR spectra and c) UV-vis diffuse reflectance spectra of GO and
224 BaFe₂O₄/rGO.

225 FTIR spectrum was recorded to verify the successful synthesis of photocatalyst. Compared the
226 spectrum of pure GO and BaFe₂O₄/rGO, the GO (Fig.1b) shows the characteristic peaks around 1734
227 cm⁻¹ (due to the presence of -COOH), 1580 cm⁻¹ (C=C vibration form graphitic domain), 1375 cm⁻¹ (-
228 C-OH), 1232 cm⁻¹ (C-O stretch) and 1050 cm⁻¹ (epoxide groups), respectively. These patterns further
229 confirm the presence of oxygen containing functional group of GO. Furthermore, a broad and less
230 intense peak in the region around 3500-3000 cm⁻¹ was also observed due to stretching vibrations of
231 hydroxyl group from absorbed water molecules or phenolic OH or OH from carboxylic groups in
232 GO. As for BaFe₂O₄/rGO (Fig.1b), the characteristic peaks of oxygen-containing functional groups of
233 GO disappear and single sharp peak appeared at band 1420.31 cm⁻¹ reveals the metal-oxygen
234 characteristic (Roonasi and Mazinani, 2017a) and reduction of GO to rGO occurred. By comparing
235 the two curves (GO and BaFe₂O₄/rGO), it was found that the characteristic peaks of GO are weakened
236 in BaFe₂O₄/rGO and confirmed the synthesis was done successfully (Sonal et al., 2020).

237 Diffusion peaks from XRD analysis of GO (Fig.1a), was found at $2\theta = 10.46^\circ$ (001) with d-spacing of
238 0.850 nm due to the oxidation of graphite. The published studies suggested that the characteristic peak
239 of graphite found at $2\theta = 26.58^\circ$ (002) would disappeared due to the addition of oxygen-containing
240 functional group (Aboubaraka et al., 2017). Thus, suggesting that GO was successfully synthesized.
241 In addition, the intensity and sharp diffraction peak was observed at $2\theta=32^\circ$ with interlayering spacing
242 0.27nm indicating the presence of metal on the surface of carbon (Roonasi and Mazinani, 2017a).
243 Besides this peak, characteristic peak of GO at $2\theta =10.46^\circ$ was disappeared and a weak peak found at
244 $2\theta = 28.43^\circ$, corresponding to coexistence of Ba²⁺ on the surface of GO in BaFe₂O₄/rGO (Fig.3a)
245 (Roonasi and Mazinani, 2017a). Therefore, the results from XRD analysis confirmed the
246 crystallographic nature of material and the coexistence of Ba²⁺ and GO.

247 XPS data used to detect the chemical constituents of GO and BaFe₂O₄/rGO. The corresponding peaks
248 of C 1s, O 1s, Ba (3d_{5/2}), (3d_{3/2}) and Ba (4d) were identified in both the sample. More specifically,
249 high-resolution of C 1s spectra of GO showed peaks at 284.6, 285.3, 288.0, and 289.2 eV (Fig.2),
250 which correspond to C-O and C=O bonds respectively (Bai et al., 2018). Additionally, with the
251 formation of BaFe₂O₄/rGO, band energies of C (1s) was decreased approximately to 284.68 eV,
252 indicating reduction of oxygen-containing functional group and confirming the transformation of GO
253 to rGO with the doping on sp² carbon atom of GO (Hu et al., 2020). Similarly, peak of O 1s found at

254 532.86 eV is attributed to the lattice of O or -OH group on the surface of GO, respectively (Hu et al.,
255 2020). While, O1s core level spectrum of BaFe₂O₄/rGO was deconvoluted at 530.68 eV (BaCO₃),
256 suggesting the presence of Ba²⁺ on the surface of GO (Han et al., 2021). This shifting of band energies
257 shows the interaction of GO and BaFe₂O₄ and their influence on the hydroxyl oxygen of the surface.
258 Evidently, the double peak of Ba (3d_{5/2}), (3d_{3/2}) and Ba (4d) appeared at binding energies of 779.60
259 eV, 794.90 eV and 89.84 eV, respectively on the surface of C1s, indicated the successful formation
260 of BaFe₂O₄/rGO (Fig.2) (Han et al., 2021).

261

262 **Fig 2:** a) Full scan spectra and extended high-resolution b) C 1s; c) O 1s and d) Ba 3d spectra of GO
263 and BaFe₂O₄/rGO

264 The surface and structural morphological were investigated by SEM and high-resolution TEM
265 (HRTEM). As shown in Fig.3a-e, GO consist of the two-dimensional, grooved and undulated sheet-
266 like structure due to deformation upon exfoliation and restacking of graphite. This inner layering of
267 GO occurs due to the presence of oxygen-containing functional groups such as carboxyl, epoxy and
268 hydroxyl group was also supported by FTIR analysis. While, BaFe₂O₄/rGO (Fig.3f-m) have smooth
269 sheet like morphology with more corrugations as compared to the GO. The elemental analysis
270 confirmed the presence of C, O and Ba in the samples with other adhering impurities and also proved
271 the successful introduction of Ba in GO (Aboubaraka et al., 2017; El-Sheikh et al., 2017; Wang et al.,
272 2012). In addition, TEM images and elemental mapping of prepared photocatalyst confirmed the
273 uniform distribution of C, O, Fe and Ba throughout the material.

274 **Fig 3:** SEM, TEM and EDS images of photocatalysts (a-e) GO; and (f-m) BaFe₂O₄/rGO.

275 The BET surface area of GO and BaFe₂O₄/rGO are 93.66 66 m²g⁻¹ and 91.50 m²g⁻¹, respectively. A
276 large surface area is widely believed to be needed for high photocatalytic process. In contrast,
277 BaFe₂O₄/rGO possess low surface area as compared to GO but shows high photocatalytic activity.
278 The possible reason was the presence of potential reactive sites and shortening of mass transfer
279 distance, enhance the adsorption and photocatalytic process (Zhu et al., 2018).

280 Therefore, this characterization studies suggested that use of GO and BaFe₂O₄/rGO proved as efficient
281 photocatalyst because various oxygen-containing functional group participates in redox reaction and
282 polyaromatic π -system of GO and BaFe₂O₄/rGO reacts with the aromatic rings of CHD in wastewater
283 by either π - π stacking interactions or strong hydrophobic effect make them highly efficient adsorbent
284 materials as well (Thakur and Kandasubramanian, 2019).

285

286 **3.2 Regression analysis for the photocatalytic activity of photocatalyst on CHD removal**

287 A polynomial model was used to represent the effects of individual parameters as well as their
288 synergistic interactive effects on the response variable in Eq. (8)-(9).

289

290 CHD removal % (GO) $\gamma = 55.34 - 2.07 X_1 + 10.16 X_2 + 4.25 X_3 - 2.26 X_1 X_2 + 0.39 X_1 X_3$ (8)
 + 0.74 $X_2 X_3 - 13.95 X_1^2 - 4.34 X_2^2 - 6.26 X_3^2$

291

292 CHD removal % (BaFe₂O₄ / rGO) = 44.67 - 1.51 $X_1 + 9.67 X_2 + 3.52 X_3 - 1.81 X_1 X_2 - 0.043 X_1 X_3$ (9)
 - 0.3 $X_2 X_3 - 11.99 X_1^2 - 3.29 X_2^2 - 1.64 X_3^2$

293

294 The results of ANOVA (Table 1) represent the suitable model for photocatalysts during photocatalysis
 295 process. The P-value of the model, for the photocatalysts, was <0.0001, and the F-value was 27.27
 296 and 63.49 for GO and BaFe₂O₄/rGO, respectively. These results confirmed that the model was highly
 297 significant, which is supported by the close agreement between the predicted and observed values
 298 (Fig.S1: A-B in supplementary material). The R² values were obtained 0.9609 and 0.9828 for GO and
 299 BaFe₂O₄/rGO, respectively, which implies high correlation between actual and predicted values for
 300 CHD removal and further confirmed the reliability of model (Sonal et al., 2018). Smaller P > F (<
 301 0.05) values show the significance of the certain model and the higher contribution towards the
 302 response variable, while the higher P-value indicates the insignificance of the model.

303 **Table 1:** ANOVA Analysis for the catalytic activity of the different photocatalyst

304

305 **3.3 Adsorption and Photocatalytic performance of prepared photocatalysts**

306 Comparison of adsorption in dark condition, photolysis and photocatalysis were carried out at RSM
 307 optimized condition (Fig.4). Adsorption studies were carried out in dark condition and remarkable
 308 results was observed with adsorption equilibrium at 80 min and 60 min for GO and BaFe₂O₄/rGO,
 309 respectively. Kinetics studies of different sample demonstrated a pseudo- second order model is better
 310 fitted with experimental and calculated results. Adsorption capacities of BaFe₂O₄/rGO and GO are
 311 303.3 mg/g (within 60 min) and 200 mg/g (within 80min), respectively. The adsorption capacity of
 312 GO enhanced by addition of BaFe₂O₄, resulted in increased surface area in BaFe₂O₄/rGO as
 313 determined by BET. However, above result indicated that BaFe₂O₄ loading was beneficial for
 314 adsorption of CHD as representative of organic pollutant. This is due to the electrostatic interaction,
 315 π - π stacking and more disorder region in BaFe₂O₄/rGO than GO (Singh et al., 2018). Point zero
 316 charge of GO (6.0) and BaFe₂O₄/rGO (4.8) (Fig.S2), this may be due to the presence of carboxyl
 317 group and metal-oxygen group in GO and BaFe₂O₄/rGO. Highest degradation rates were observed,
 318 when solution pH was equal to alkaline condition due to the electrostatic interaction occur among
 319 cationic nature of CHD and positively charged photocatalyst. Thus, adsorption occurs due to the
 320 electrostatic interaction of pollutant on the surface of photocatalysts, making good agreement for
 321 adsorption of antibiotics.

322 **Fig 4:** a) Adsorption of CHD at optimized condition; b) pseudo-first order model; and c) pseudo-
 323 second order model for GO and BaFe₂O₄/rGO

324 In addition, agglomeration and surface hydrophobicity are the major limitation for modification of
325 GO and several researches were conducted to modified surface of GO via doping, fabrication, or
326 immobilization for improvisation of these shortcomings. Therefore, grafting of Ba²⁺ on the surface of
327 GO aimed to realize separation, dispersity, high antibiotics adsorption capacity (Li et al., 2019).

328
329 The photodegradation efficiency of both materials were compared under visible light irradiation for
330 CHD (Fig.5a). First, blank experiment (photolysis) was performed in visible-light (370-420 nm) and
331 slight degradation of CHD (10%). The adsorption-desorption equilibrium experiment was carried out
332 in dark for stability of the photocatalytic reaction. It was observed that photocatalyst showed
333 negligible degradation in absent of light. Moreover, it was found that the increased adsorption
334 efficiency could also be favourable for photocatalytic activity i.e., GO (88.17%) and BaFe₂O₄/rGO
335 (93.95%) for CHD removal. Since, adsorption process decreased the mass transfer distance among
336 pollutant and photocatalyst. Meanwhile, narrow band-gap energy, homogeneous dispersion, and
337 excellent electrical conductivity leading to the significant interaction of d-d (from 3d orbital of Ba
338 ions) and d- π transitions (aromatic rings of CHD molecules) under visible-light formed by
339 photogenerated carrier with short time and pollutant. Additionally, pseudo-first order (PFO) kinetics
340 was in good agreement with reaction rate constant 0.954 (GO) and 1.14 (BaFe₂O₄/rGO), respectively.
341 While correlation coefficient of the model (PFO) are 0.937(GO) and 0.984 (BaFe₂O₄/rGO),
342 respectively i.e. closer to 1.

343 Reusability test carried out to investigate the large-scale applicability of photocatalyst as an industrial
344 use. The rate of CHD degradation by BaFe₂O₄/rGO decreased after 4 cycles, indicating that
345 BaFe₂O₄/rGO possessed good reusability.

346 Thus, above results suggested the BaFe₂O₄/rGO showed optimal balance for adsorption and
347 photocatalytic process as compared to the GO and also considered as durable photocatalyst.

348

349 **Fig 5:** a) Photocatalytic degradation of CHD at optimized condition; b) pseudo-first order kinetics; c)
350 trapping experiment of active species; and d) reusability experiment of GO and BaFe₂O₄/rGO
351 mediated photocatalytic degradation of CHD.

352 **3.4 Probable mechanism for CHD degradation**

353 Charge separations occur on the surface of photocatalysts (GO and BaFe₂O₄/rGO) by exposure of
354 visible-light irradiation. The photogenerated electron and photogenerated holes migrates to the surface
355 of photocatalyst, where they participate in redox reaction for degradation of targeted pollutant. As
356 photodegradation efficiency of photocatalyst is related to the contribution of its active radicals
357 (Fig.5c). A series of trapping experiments were carried out and isopropanol (IPA) (1%), 1.0 mM of
358 potassium persulfate (K₂S₂O₈) and ethylenediaminetetraacetic acid (EDTA) were used as scavengers
359 of hydroxyl radicals (^oOH), electron (e⁻), and holes (h⁺) respectively. The photocatalytic efficiency of

360 GO and BaFe₂O₄/rGO was reduced by addition of IPA and K₂S₂O₈ and insignificant change was
361 observed on EDTA addition. However, °OH and e⁻ actively participate in photocatalytic degradation
362 of CHD in GO and BaFe₂O₄/rGO mediated photocatalytic reaction but h⁺ has insignificant effect,
363 respectively. The removal rate reduced from 88.17 % to 67.44 (IPA),55.81(EDTA) in the case of GO
364 mediated photocatalysis process, while in BaFe₂O₄/rGO mediated photodegradation of CHD
365 decreased rapidly from 93.95 % to 75.19% (IPA) and 63.56% (EDTA), respectively. This result
366 indicates that IPA and K₂S₂O₈ inhibited the CHD degradation and further confirms that °OH and e⁻
367 was dominating reactive species. Above result speculated the effect of photogenerated reactive
368 species decreased in order of e⁻ > °OH > h⁺.

369 The photogenerated electron (valance band) and holes (conduction band) participate in redox reaction,
370 where holes may react with water molecules or OH⁻ to produce °OH and photogenerated electron at
371 conduction band may reacts with oxygen to produce superoxide radical anions (O₂⁻) (Fig.5c). As CHD
372 (cationic in nature) reacts with °OH and e⁻, then oxidation process takes place in degradation of
373 pollutant.

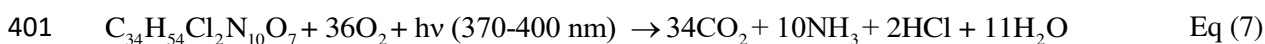
374 Performance and application of the any catalyst depends on degradation and mineralization of the
375 targeted compound into nontoxic smaller molecules. Therefore, it is important to understand the CHD
376 degradation to 88.17 % (GO) and 93.95 % (BaFe₂O₄/rGO) by:

377
378 a) TOC determination, which shows the relationship between mineralization of pollutant and b)
379 formation of its by-products. The TOC values were reduced to 79.21% and 88.14% for GO and GO-
380 BaFe₂O₄/rGO, respectively showing the extent of mineralization taking place in the reaction solution
381 (Fig.6a). Difference in the values of TOC reduction and degradation of CHD, reflects the presence of
382 carbon atom as by-products in treated water (Chen et al., 2020). This result supported with reduction
383 in hydrophobic compound and conversion of heteroatoms such as chlorine or nitrogen into inorganic
384 anions in solution was also determined to investigate the photocatalytic efficiency of catalysts. UV₂₅₄
385 is the crucial parameter to determine the cleavage of aromatic C=C in solution after photocatalysis
386 process. Thus, reduction in the value of aromatic C=C content present in CHD with respect to time
387 was measured at 254 nm in UV-Spectroscopy (Priya et al., 2018). UV₂₅₄ reduction was ranging from
388 1.369 to 0.668 and 0.397 for GO and BaFe₂O₄/rGO, respectively. This reduction is stoichiometrically
389 close to the removal percentage of hydrophobic compound using (GO) 57.19 % and 71.09%
390 (BaFe₂O₄/rGO) (Fig.6b). Hence, UV₂₅₄ reduction confirm the breakdown of long chain carbon atoms
391 into smaller molecules. But 57.19 % in GO mediated treatment indicates that breakdown of CHD into
392 transformed product i.e.p-chloroaniline validated by LC/MS has adverse effect on aquatic life than
393 parent compound .Similarly, inorganic ions production and TOC reduction supports the results of
394 UV₂₅₄ reduction. From this, it could be hypothesized that oxidative mechanism of photocatalysis
395 process participate in cleavage of the aromatic ring of CHD molecules (Schneider et al., 2014).

396 Therefore, result showed that GO and BaFe₂O₄/rGO also has immense potential to reduce aromaticity
397 of the solution.

398 The overall reaction during photo mineralization of CHD in the excess of oxygen under optimized
399 experimental condition is validated by the equation given below:

400



402

403 Besides the TOC and aromaticity reduction, in order to explicate the route of CHD conversion into
404 intermediates of the reaction, the sample was subjected to various experimental condition concerning
405 i) the presence of chloride ion in the reaction mixture, ii) release of attached nitrogen into ammonia
406 ion.

407 **Fig 6:** a) TOC removal and b) UV absorbance reduction in GO and BaFe₂O₄/rGO mediated
408 photocatalytic degradation of CHD at optimized condition.

409 The initial concentration-time profiles of chloride anion and inorganic nitrogen (NH₄⁺) for
410 photocatalytic system shows significant conversion of organic chlorine to chloride anion in GO and
411 BaFe₂O₄/rGO mediated CHD removal. It was observed that there was a formation of approximately,
412 0.7748 mg/L and 0.7814 mg/L chloride ion respectively, in the reaction matrix of GO and
413 BaFe₂O₄/rGO treated water. A similar trend was also observed for the attached nitrogen where,
414 75.96% and 78.56% N-NH₃ (stoichiometric amount) formation was observed in the case of GO and
415 BaFe₂O₄/rGO treated wastewater, respectively.

416

417 b) Secondly, bacterial susceptibility test was carried out regarding the toxicity of intermediate. For
418 toxicological studies of intermediate compound targeted microorganism was *Bacillus cereus*, which is
419 commonly residing in human oral cavities was subjected to antimicrobial susceptibility test for
420 toxicity investigation of the intermediate compound. Kirby–Bauer Disk Diffusion method was used to
421 demonstrate toxicological results of the degraded compound. The zone of inhibition (measured in
422 millimetres) of the treated sample through photocatalysts were observed on their respective plates.
423 The diameter of the inhibition zone related to the susceptibility of *Bacillus cereus* and the diffusion
424 rate of pure sample to the antibiotics such as amoxicillin and ciprofloxacin through agar media.
425 Inhibition zone of a standard solution of CHD, 30 mg/L concentration of sample, ciprofloxacin and
426 amoxicillin antibiotics was 30 mm, 15 mm, 50 mm and 3 mm in diameter (Fig.S3). Negligible
427 inhibition zone was observed for the degraded product after photocatalytic degradation of CHD. The
428 pattern of inhibition zone found after preliminary toxicological test on microorganisms without any
429 preclinical analysis of CHD, illustrates the superiority of antimicrobial activity of pure CHD over
430 ciprofloxacin and amoxicillin. From toxicological studies, it was observed that disposal of treated

431 water into the environment was non-toxic in nature or unlikely to cause any harmful effect on the
432 aquatic ecosystem.

433 Hence, formation of these mineralized products as well as degradation rate of CHD indicates the
434 extent of true mineralization process. Higher degradation of CHD was achieved using BaFe₂O₄/rGO
435 as compared to GO, this could be due to the dispersion of photocatalyst in water and enough
436 availability of active site to irradiate through visible light led to the generation of enough °OH for
437 noticeable mineralization of CHD. This stoichiometrically estimated values of formed chloride anion
438 is close to the chlorine attached to the ring of CHD in untreated water (1.438 mg/L). Therefore, this
439 estimation degraded products such as chloride ion or nitrogen moieties validates the mineralization of
440 CHD by chloride ion formation.

441 In this context, degraded product analysis was carried out by LC-MS spectroscopy. Spectral peaks
442 reflect the main intermediate formed during degradation of CHD and thus the toxicological
443 investigation of degraded products has been carried out. The spectral reflection of pure chlorhexidine
444 at 505 and 507 m/z shows two isotopes of Cl atoms (35 and 37) present in the structure.

445 Whereas in case of GO, fragmentation of the parent molecules into smaller molecules represented by
446 spectral peak (m/z = 127) with some noise shows the reduced number of byproducts, confirming 75-
447 79% of the mineralization process. In BaFe₂O₄/rGO mediated photocatalytic degradation,
448 fragmentation of CHD into intermediates represented by one minor peaks (m/z = 149) with reduced
449 number of intermediates (Table 2). A possible pathway for degradation of CHD by catalysts was
450 proposed and breakdown of biguanide moiety found as a major contributor for the mineralization of
451 CHD. Due to the breakdown of biguanide moiety, hydrolytically sensitive group of CHD involves the
452 hydration and subsequent cleavage of C=N bond which leads to the conversion of parent compound to
453 transformed products. In addition, quantification and mass identification of transformed product are
454 beyond the scope of study and would hopefully be addressed in a future study.

455 **Table 2:** LCMS Analysis of GO and BaFe₂O₄/rGO mediated photocatalytic degradation of CHD.

456 ***3.6 Evaluation of photocatalytic efficiency of catalysts in UV and solar treatment.***

457 To evaluate the efficiency of photocatalyst with ultimate goal of solar treatment for removal of
458 organic pollutant. For this purpose, GO and BaFe₂O₄/rGO were used for CHD removal under solar as
459 well as UV-light. First, photodegradation were carried out under the UV-irradiation and solar light at
460 RSM optimized condition for the sake comparison with visible-treatment (Wang et al., 2019). These
461 results justify the remarkable potential of photocatalysts for degradation of CHD using solar light to
462 maintain the sustainability. The removal efficiency of GO and BaFe₂O₄/rGO for CHD degradation
463 under solar irradiation in terms of UV absorbance and TOC showed in (Table 3). The results
464 highlighted the superior performance under UV light as compared to solar as well as visible. Thus,
465 solar possess combination of UV and visible was beneficial to accelerate the removal of such

466 recalcitrant pollutant. Energy consumption and economics are of paramount importance for treatment
467 technologies.

468 **Table 3:** Comparison of CHD degradation using GO and BaFe₂O₄/rGO under different source of
469 light.

470 **3.7. Electrical energy consumption**

471 Electrical energy consumption is also one of the important factors for selection of water treatment
472 technology and its industrial applicability. Since photocatalytic degradation is an electric-intensive
473 process for the removal of recalcitrant organic pollutant. Although, consumption of electrical energy
474 is major representative of operating cost, quality goal and economics on large-scale. In this work,
475 efficiency of treatment process based on electrical energy consumption was quantified using the
476 concept of figure-of-merit electrical energy per order (Eq.-6). For visible treatment, the calculated
477 EEO for GO mediated photodegradation was in the range of 20.09-29.95 (kW h L⁻¹ order⁻¹), which
478 shows more consumption than BaFe₂O₄/rGO mediated visible treatment (16.08 to 22.79 kWhL⁻¹order⁻¹).
479 Above results show that BaFe₂O₄/rGO is more energy efficient than GO, reason could be more
480 reactive site and generation of radical for photodegradation of such low concentration organic
481 pollutant. For solar driven system, energy efficiency was quantified during UV treatment. Evidently,
482 EEO of GO and BaFe₂O₄/rGO was ranging from 0.59 to 1.71 kW h L⁻¹ order⁻¹ and 0.76 to 1.14 kW h
483 L⁻¹ order⁻¹, respectively. This higher EEO values of visible treatment could enhance the efficiency of
484 solar treatment (45% visible and 4% UV) (Santiago-Morales et al., 2013). Additionally, reusability of
485 GO and BaFe₂O₄/rGO was also investigated, and results were showed good stability even after 3 cycle
486 of BaFe₂O₄/rGO (Fig.5d).

487

488 **4. Conclusion**

489 In this study, synthesized BaFe₂O₄/rGO showed enhanced catalytic activity for degradation of CHD in
490 comparison to GO. The structural properties were affected by doping of Ba²⁺ showed decreased band
491 energy of catalyst, which enhanced the photocatalytic degradation of CHD. Characterization results
492 (EDS, XPS and XRD) confirm the crystallinity of the structure and doping on the surface of sample
493 that may favour the photocatalytic degradation of CHD by separation of charge carrier. The result of
494 kinetic studies showed that pseudo first order kinetic model was well fitted, based on the rate constant
495 and R² values. The trapping experiment tests demonstrated that the major reactive oxygen species
496 are *OH radicals and photogenerated electrons for CHD degradation. Based on intermediate analysis
497 as well as reduction in TOC and UV₂₅₄, it was observed that GO and BaFe₂O₄/rGO decompose
498 complex long chain into shorter chain species, thus their bacterial toxicity was also reduced during
499 photocatalysis process. The efficiency of as prepared catalyst was examined in the use of energy and
500 the results are higher than previous studies due to the removal of refractory pollutant in the lower

501 concentration. But comparative studies demonstrated that BaFe₂O₄/rGO would be the potential
502 catalyst for solar-driven photocatalysis and maintain the sustainability. Overall results suggested that
503 application of modified BaFe₂O₄/rGO photocatalyst for removal and efficient degradation of
504 antibiotic pollutants could be achieved through adsorption and photocatalysis approach. Thus, the
505 practical applicability of this catalyst could be exploited for significant removal of hydrophobic
506 organic pollutant form others industrial wastewater.

507

508 **Acknowledgement:**

509 The authors are very thankful for the financial support from Indian Institute of Technology (Indian
510 School of Mines), Dhanbad under a Junior Research Fellowship scheme funded by Ministry of
511 Human Resource Development (MHRD), Government of India, New Delhi to carry out this research
512 work. We would also like to acknowledge Aneek Kulia and Soni Kumari for their valuable time in
513 data interpretation and formatting of the manuscript and Nanotechnology Research Centre (NRC),
514 SRMIST for providing the instrumentation facilities.

515

516 **Ethics approval and consent to participate.**

517 Not applicable

518

519 **Consent for publication**

520 Not applicable

521

522 **CRedit authorship contribution statement**

523 **Ms. Astha Singh:** All experiment, analysis and interpretation of results, Conceptualization,
524 Methodology, Investigation, Formal analysis & Writing-Original Draft. (First Author)

525 **Prof. Brijesh Kumar Mishra:** Supervision, Conceptualization, Review &Editing. (Corresponding
526 Author)

527

528 **Funding**

529 Funding information is not applicable.

530

531 **Competing interests**

532 The authors declare that they have no competing interests.

533

534 **Availability of data and materials**

535 All data generated or analysed during this study are included in this published article [and its
536 supplementary information files].

537

538

539 **Declaration of competing interest**

540

541 The authors declare that they have no known competing financial interests or personal relationships
542 that could have appeared to influence the work reported in this paper.

543

544

545 **5. References**

546 Aboubaraka, A.E., Aboelfetoh, E.F., Ebeid, E.Z.M., 2017. Coagulation effectiveness of graphene
547 oxide for the removal of turbidity from raw surface water. *Chemosphere* 181, 738–746.

548 <https://doi.org/10.1016/j.chemosphere.2017.04.137>

549 Azarpira, H., Sadani, M., Abtahi, M., Vaezi, N., Rezaei, S., Atafar, Z., Mohseni, S.M., Sarkhosh, M.,

550 Ghaderpoori, M., Keramati, H., Hosseini Pouya, R., Akbari, A., fanai, V., 2019. Photo-catalytic

551 degradation of triclosan with UV/iodide/ZnO process: Performance, kinetic, degradation

552 pathway, energy consumption and toxicology. *J. Photochem. Photobiol. A Chem.* 371, 423–432.

553 <https://doi.org/10.1016/j.jphotochem.2018.10.041>

554 Bai, X., Du, Y., Hu, X., He, Y., He, C., Liu, E., Fan, J., 2018. Synergy removal of Cr (VI) and organic

555 pollutants over RP-MoS₂/rGO photocatalyst. *Appl. Catal. B Environ.* 239, 204–213.

556 <https://doi.org/10.1016/j.apcatb.2018.08.016>

557 Casbeer, E., Sharma, V.K., Li, X.Z., 2012. Synthesis and photocatalytic activity of ferrites under

558 visible light: A review. *Sep. Purif. Technol.* 87, 1–14.

559 <https://doi.org/10.1016/j.seppur.2011.11.034>

560 Chen, Y., Zhang, X., Wang, L., Cheng, X., Shang, Q., 2020. Rapid removal of phenol/antibiotics in

561 water by Fe-(8-hydroxyquinoline-7-carboxylic)/TiO₂ flower composite: Adsorption combined

562 with photocatalysis. *Chem. Eng. J.* 402. <https://doi.org/10.1016/j.cej.2020.126260>

563 Das, R., Sarkar, S., Bhattacharjee, C., 2014. Photocatalytic degradation of chlorhexidine-A chemical

564 assessment and prediction of optimal condition by response surface methodology. *J. Water*

565 *Process Eng.* 2, 79–86. <https://doi.org/10.1016/j.jwpe.2014.05.005>

566 El-Sheikh, S.M., Khedr, T.M., Hakki, A., Ismail, A.A., Badawy, W.A., Bahnemann, D.W., 2017.

567 Visible light activated carbon and nitrogen co-doped mesoporous TiO₂ as efficient photocatalyst

568 for degradation of ibuprofen. *Sep. Purif. Technol.* 173, 258–268.

569 <https://doi.org/10.1016/j.seppur.2016.09.034>

570 Fidelis, M.Z., Abreu, E., Dos Santos, O.A.A., Chaves, E.S., Brackmann, R., Dias, D.T., Lenzi, G.G.,

571 2019. Experimental design and optimization of triclosan and 2,8-dichlorodibenzo-p-dioxin
572 degradation by the Fe/Nb₂O₅/UV system. *Catalysts* 9, 1–18.
573 <https://doi.org/10.3390/catal9040343>

574 Han, J.K., Song, D.S., Lim, Y.R., Song, W., Myung, S., Lee, S.S., An, K.S., Jung, H.K., Santucci, S.,
575 Esposito, V., Lim, J., 2021. In-depth exploration of the synergistic interplay between perovskite
576 barium titanate nanoparticles and two-dimensional graphene oxide for flexible piezoelectric
577 nanogenerators. *Appl. Surf. Sci.* 538, 147962. <https://doi.org/10.1016/j.apsusc.2020.147962>

578 Hu, Z., Ge, M., Guo, C., 2020. Efficient removal of levofloxacin from different water matrices via
579 simultaneous adsorption and photocatalysis using a magnetic Ag₃PO₄/rGO/CoFe₂O₄ catalyst.
580 *Chemosphere* 128834. <https://doi.org/10.1016/j.chemosphere.2020.128834>

581 Li, M. fang, Liu, Y. guo, Zeng, G. ming, Liu, N., Liu, S. bo, 2019. Graphene and graphene-based
582 nanocomposites used for antibiotics removal in water treatment: A review. *Chemosphere* 226,
583 360–380. <https://doi.org/10.1016/j.chemosphere.2019.03.117>

584 Nasseh, N., Taghavi, L., Barikbin, B., Nasser, M.A., 2018. Synthesis and characterizations of a novel
585 FeNi₃/SiO₂/CuS magnetic nanocomposite for photocatalytic degradation of tetracycline in
586 simulated wastewater. *J. Clean. Prod.* 179, 42–54. <https://doi.org/10.1016/j.jclepro.2018.01.052>

587 Nidhi, K., Indrajeet, S., Khushboo, M., Gauri, K., Sen, D.J., 2011. Hydrotropy: A promising tool for
588 solubility enhancement: A review. *Int. J. Drug Dev. Res.* 3, 26–33. <https://doi.org/10.1002/jps>

589 Priya, T., Prakash, P., Mishra, B.K., 2018. Understanding the coagulant activity of zirconium
590 oxychloride to control THMs formation using response surface methodology. *Ecotoxicol.*
591 *Environ. Saf.* 159, 28–37. <https://doi.org/10.1016/j.ecoenv.2018.04.036>

592 Roonasi, P., Mazinani, M., 2017a. Synthesis and application of barium ferrite/activated carbon
593 composite as an effective solar photocatalyst for discoloration of organic dye contaminants in
594 wastewater. *J. Environ. Chem. Eng.* 5, 3822–3827. <https://doi.org/10.1016/j.jece.2017.07.035>

595 Roonasi, P., Mazinani, M., 2017b. Synthesis and application of barium ferrite/activated carbon
596 composite as an effective solar photocatalyst for discoloration of organic dye contaminants in
597 wastewater. *J. Environ. Chem. Eng.* 5, 3822–3827. <https://doi.org/10.1016/j.jece.2017.07.035>

598 Santiago-Morales, J., Gómez, M.J., Herrera-López, S., Fernández-Alba, A.R., García-Calvo, E.,
599 Rosal, R., 2013. Energy efficiency for the removal of non-polar pollutants during ultraviolet
600 irradiation, visible light photocatalysis and ozonation of a wastewater effluent. *Water Res.* 47,
601 5546–5556. <https://doi.org/10.1016/j.watres.2013.06.030>

602 Schneider, J., Matsuoka, M., Takeuchi, M., Zhang, J., Horiuchi, Y., Anpo, M., Bahnemann, D.W.,
603 2014. Understanding TiO₂ Photocatalysis: Mechanisms and Materials. *Chem. Rev.* 114, 9919–
604 9986. <https://doi.org/10.1021/cr5001892>

605 Singh, M., Kaushal, S., Singh, P., Sharma, J., 2018. Boron doped graphene oxide with enhanced
606 photocatalytic activity for organic pollutants. *J. Photochem. Photobiol. A Chem.* 364, 130–139.

607 <https://doi.org/10.1016/j.jphotochem.2018.06.002>

608 Sonal, S., Prakash, P., Mishra, B.K., Nayak, G.C., 2020. Synthesis, characterization and sorption
609 studies of a zirconium(IV) impregnated highly functionalized mesoporous activated carbonsb.
610 RSC Adv. 10, 13783–13798. <https://doi.org/10.1039/c9ra10103a>

611 Sonal, S., Singh, A., Mishra, B.K., 2018. Decolorization of reactive dye Remazol Brilliant Blue R by
612 zirconium oxychloride as a novel coagulant: Optimization through response surface
613 methodology. Water Sci. Technol. 78, 379–389. <https://doi.org/10.2166/wst.2018.307>

614 Sousa, C.P., de Oliveira, R.C., Freire, T.M., Fechine, P.B.A., Salvador, M.A., Homem-de-Mello, P.,
615 Morais, S., de Lima-Neto, P., Correia, A.N., 2017. Chlorhexidine digluconate on chitosan-
616 magnetic iron oxide nanoparticles modified electrode: Electroanalysis and mechanistic insights
617 by computational simulations. Sensors Actuators, B Chem. 240, 417–425.
618 <https://doi.org/10.1016/j.snb.2016.08.181>

619 Thakur, K., Kandasubramanian, B., 2019. Graphene and Graphene Oxide-Based Composites for
620 Removal of Organic Pollutants: A Review. J. Chem. Eng. Data 64, 833–867.
621 <https://doi.org/10.1021/acs.jced.8b01057>

622 Wang, H., Zhang, M., He, X., Du, T., Wang, Y., Li, Y., Hao, T., 2019. Facile prepared ball-like TiO₂
623 at GO composites for oxytetracycline removal under solar and visible lights. Water Res. 160,
624 197–205. <https://doi.org/10.1016/j.watres.2019.05.073>

625 Wang, X., Xu, G., Tu, Y., Wu, D., Li, A., Xie, X., 2021. BiOBr/PBCD-B-D dual-function catalyst
626 with oxygen vacancies for Acid Orange 7 removal: Evaluation of adsorption-photocatalysis
627 performance and synergy mechanism. Chem. Eng. J. 411, 128456.
628 <https://doi.org/10.1016/j.cej.2021.128456>

629 Wang, Z.L., Xu, D., Huang, Y., Wu, Z., Wang, L.M., Zhang, X.B., 2012. Facile, mild and fast
630 thermal-decomposition reduction of graphene oxide in air and its application in high-
631 performance lithium batteries. Chem. Commun. 48, 976–978.
632 <https://doi.org/10.1039/c2cc16239c>

633 Yuan, Q., Zhang, D., Yu, P., Sun, R., Javed, H., Wu, G., Alvarez, P.J.J., 2020. Selective Adsorption
634 and Photocatalytic Degradation of Extracellular Antibiotic Resistance Genes by Molecularly-
635 Imprinted Graphitic Carbon Nitride. Environ. Sci. Technol. 54, 4621–4630.
636 <https://doi.org/10.1021/acs.est.9b06926>

637 Zhang, X., Shen, J., Zhuo, N., Tian, Z., Xu, P., Yang, Z., Yang, W., 2016. Interactions between
638 Antibiotics and Graphene-Based Materials in Water: A Comparative Experimental and
639 Theoretical Investigation. ACS Appl. Mater. Interfaces 8, 24273–24280.
640 <https://doi.org/10.1021/acsami.6b09377>

641 Zhu, C., Chen, X., Ma, J., Gu, C., Xian, Q., Gong, T., Sun, C., 2018. Carbon Nitride-Modified
642 Defective TiO₂-x@Carbon Spheres for Photocatalytic H₂ Evolution and Pollutants Removal:

643 Synergistic Effect and Mechanism Insight. *J. Phys. Chem. C* 122, 20444–20458.
644 <https://doi.org/10.1021/acs.jpcc.8b06624>
645 Zwiener, C., Frimmel, F.H., 2000. Oxidative treatment of pharmaceuticals in water. *Water Res.* 34,
646 1881–1885. [https://doi.org/10.1016/S0043-1354\(99\)00338-3](https://doi.org/10.1016/S0043-1354(99)00338-3)
647

Figures

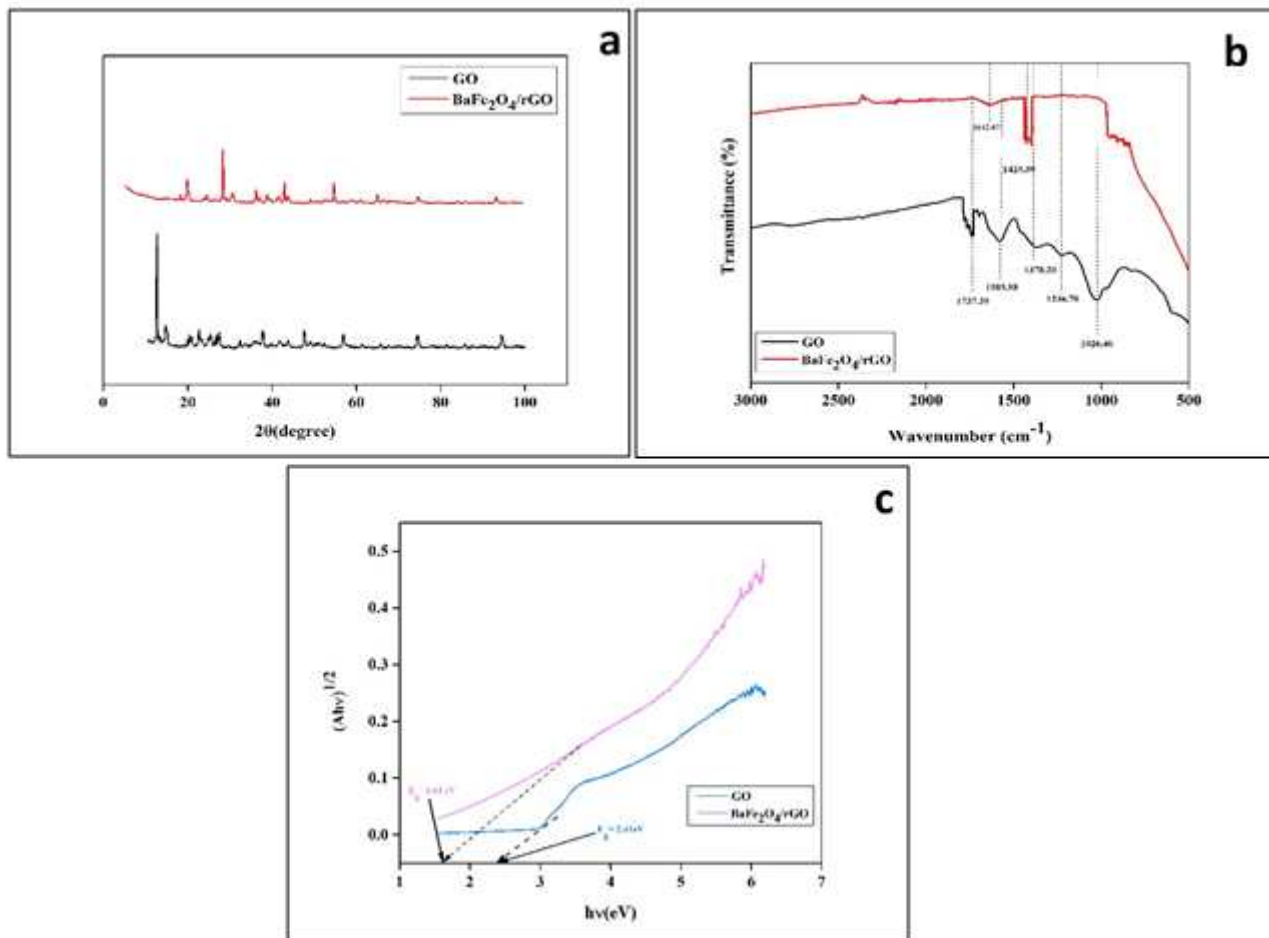


Figure 1

a) XRD patterns; b) FTIR spectra and c) UV-vis diffuse reflectance spectra of GO and BaFe₂O₄/rGO.

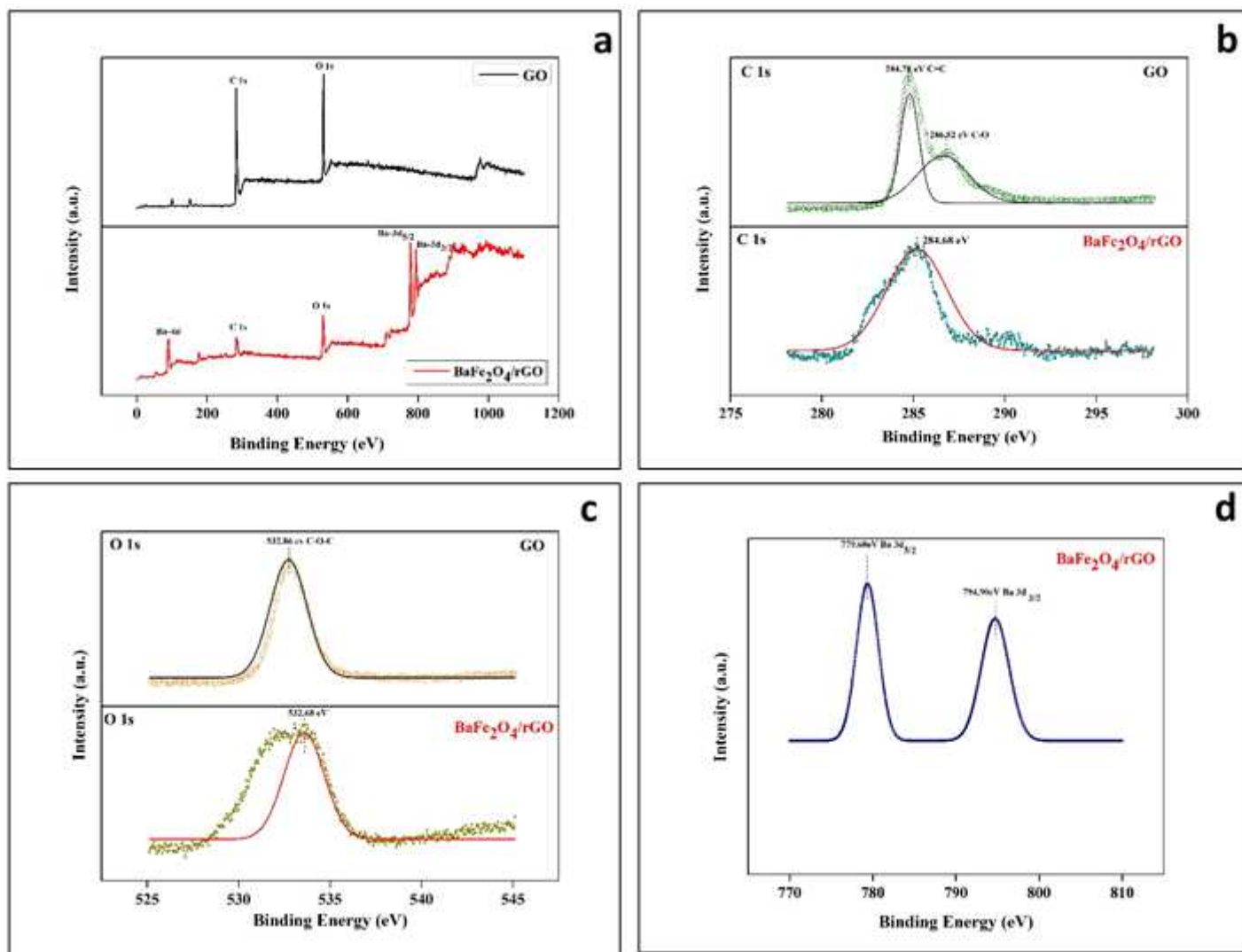


Figure 2

a) Full scan spectra and extended high-resolution b) C 1s; c) O 1s and d) Ba 3d spectra of GO and BaFe₂O₄/rGO.

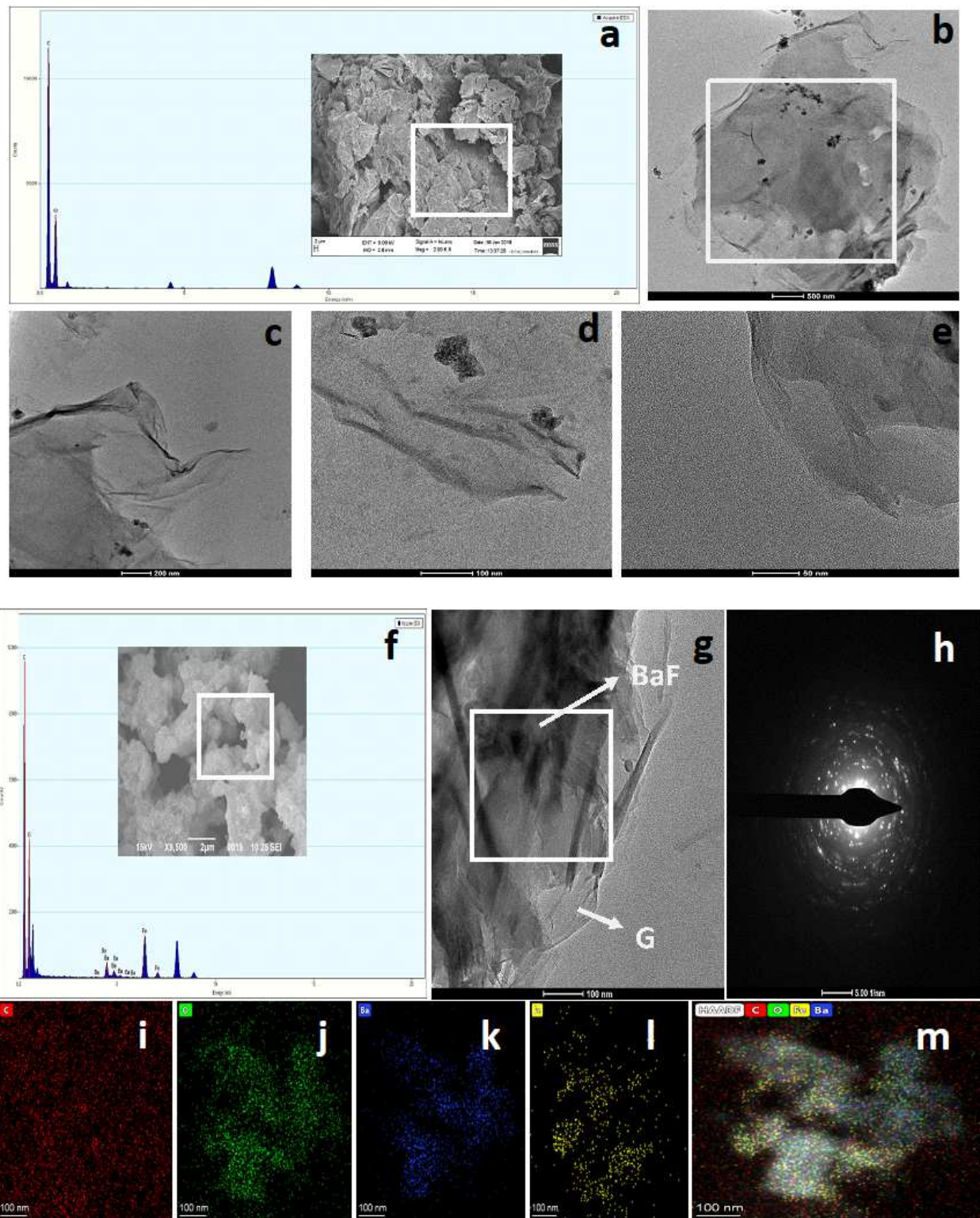


Figure 3

SEM, TEM and EDS images of photocatalysts (a-e) GO; and (f-m) BaFe₂O₄/rGO.

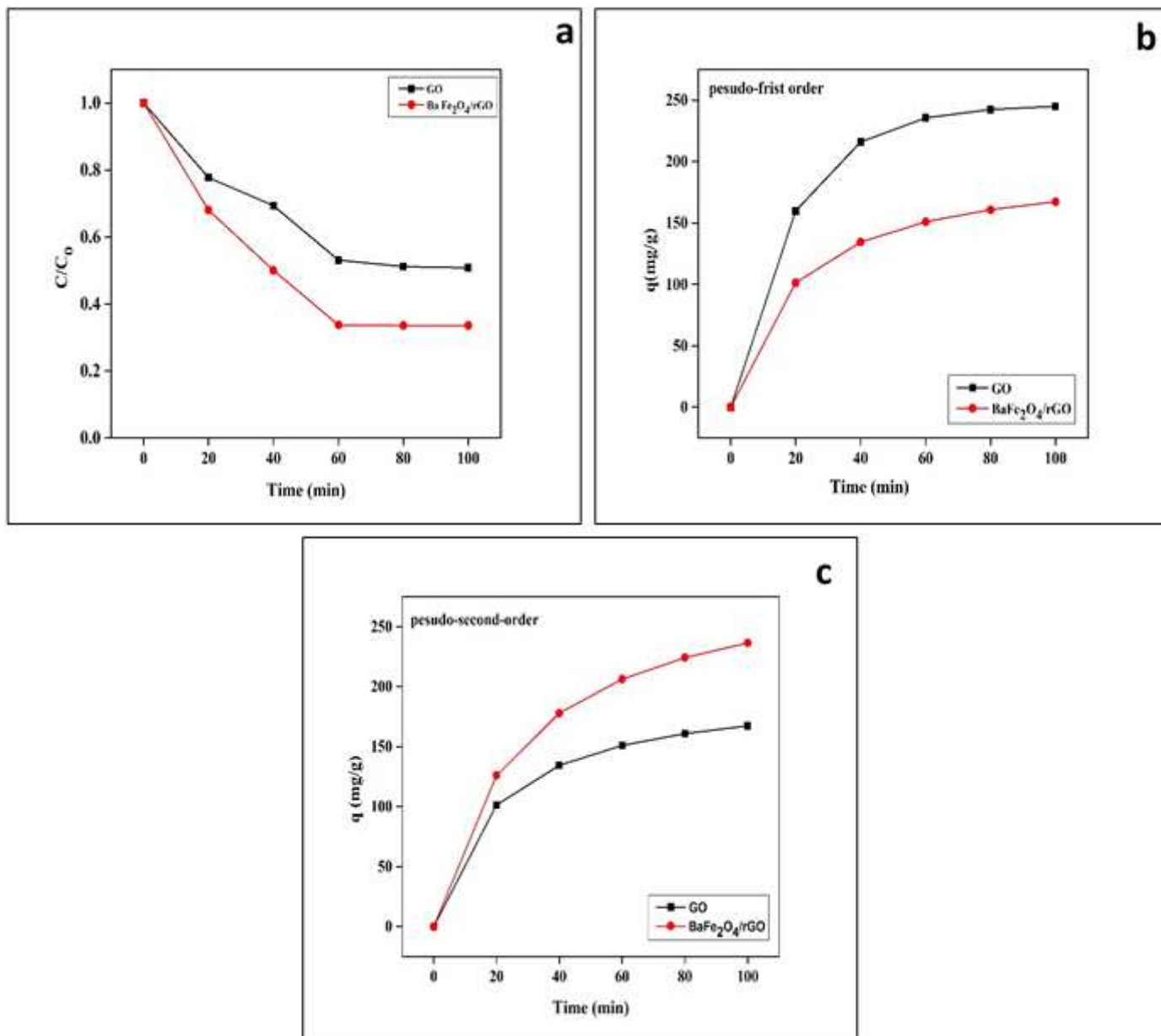


Figure 4

a) Adsorption of CHD at optimized condition; b) pseudo-first order model; and c) pseudo-second order model for GO and BaFe₂O₄/rGO.

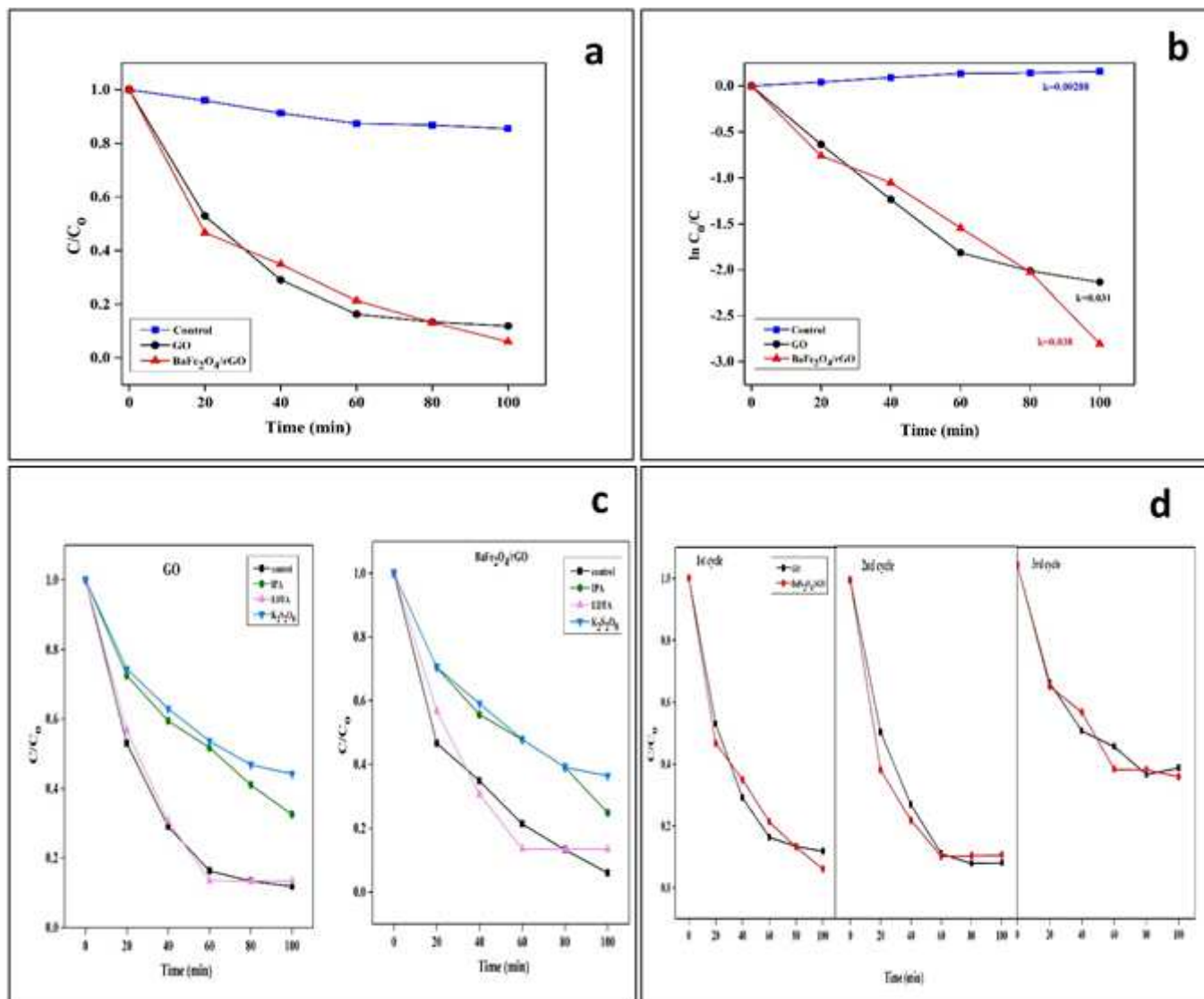


Figure 5

a) Photocatalytic degradation of CHD at optimized condition; b) pseudo-first order kinetics; c) trapping experiment of active species; and d) reusability experiment of GO and $BaFe_2O_4/rGO$ mediated photocatalytic degradation of CHD.

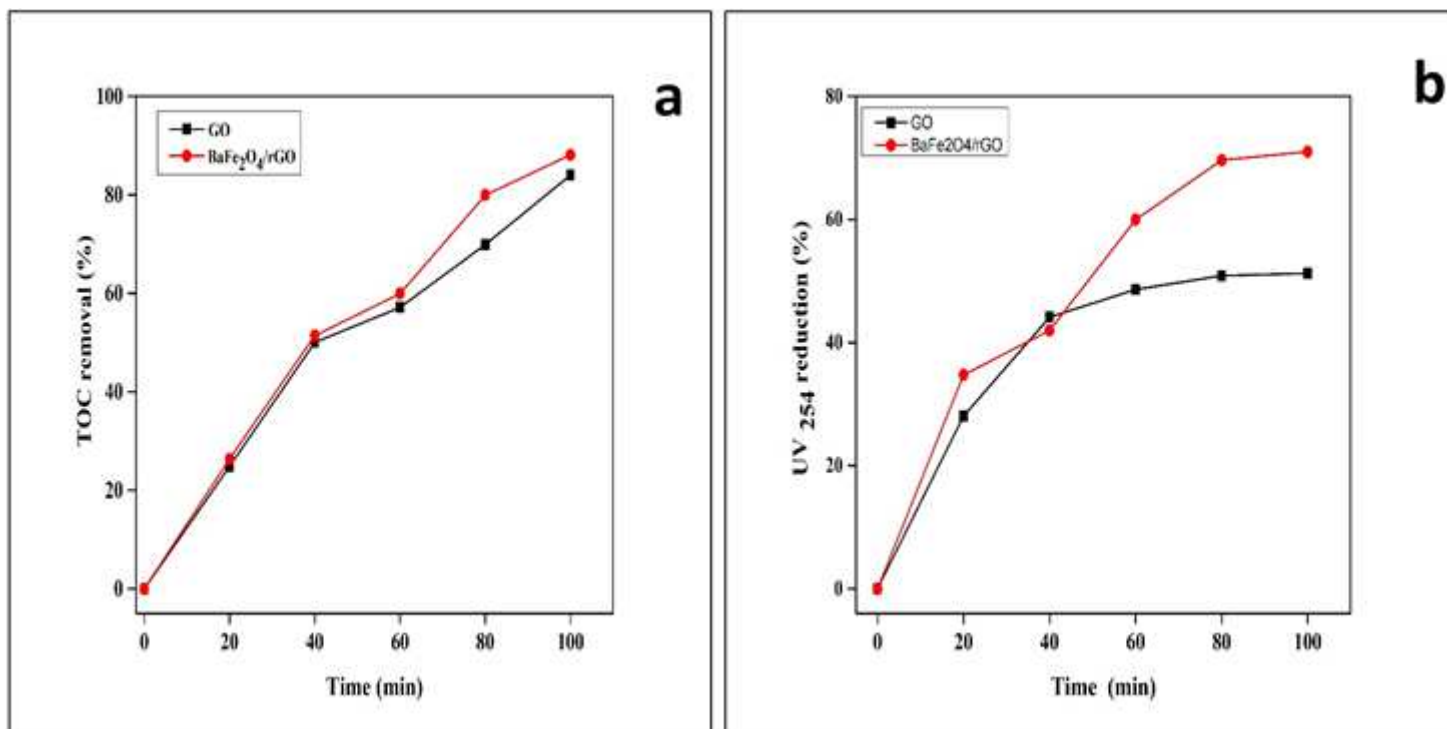


Figure 6

a) TOC removal and; b) UV absorbance reduction in GO and BaFe₂O₄/rGO mediated photocatalytic degradation of CHD at optimized condition.

Supplementary Files

This is a list of supplementary files associated with this preprint. Click to download.

- [GA.png](#)
- [Supplementary.docx](#)